J. Appl. Comput. Mech., 11(1) (2025) 39-54
DOI: 10.22055/jacm.2024.46204.4480

ISSN: 2383-4536
jacm.scu.ac.ir

Shahid Chamran
University of Ahvaz

Journal of
Applied and Computational Mechanics

Research Paper

Effect of Splitter Angles on Characteristics of Mixing Layer Flow: A Numerical Study

Trung Dung Nguyen[1], Dinh Anh Le[2], Van Minh Do[3], Anh Tuan Nguyen[1], The Hung Tran[1]

[1] Faculty of Aerospace Engineering, Le Quy Don Technical University, 236 Hoang Quoc Viet, Bac Tu Liem, Hanoi, Vietnam,
Email: trungdungcfd.work@gmail.com (T.D.N.); anhtuannguyen2410@gmail.com (A.T.N.); tranthehung_k24@lqdtu.edu.vn (T.H.T.)

[2] School of Aerospace Engineering, University of Engineering and Technology, Vietnam National University (Hanoi), Hanoi, Vietnam, Email: anh.ld@vnu.edu.vn

[3] Faculty of Special Equipment, Le Quy Don Technical University, 236 Hoang Quoc Viet, Bac Tu Liem, Hanoi, Vietnam, Email: minhdv100@gmail.com

Received February 22 2024; Revised May 20 2024; Accepted for publication May 22 2024.
Corresponding author: T.H. Tran (tranthehung_k24@lqdtu.edu.vn)

Abstract. This study investigates the effect of splitter angles on the aerodynamic flow of two free streams under incompressible conditions. The angle of the splitter is changed from 0 to 40° to simulate different wake structures on the slant. The convective Mach number was selected at 0.185. The velocities at the upper surface (primary freestream) and lower surface (secondary freestream) are changed to generate two different cases. The simulation was conducted using steady generalized k-ω (GEKO) models with modification of mixing coefficients and large eddy simulation for transient flows. The results of numerical data were validated with experimental data with the same flow conditions. This study presents that when initial parameters are suitably selected, the numerical schemes provide sufficient accurate averaged results. For case 1, when the primary freestream is higher, the length of the mixing region increases with the splitter angle. Additionally, the generation of the wake flow leads to movement upward of the mixing position for splitter angles above 20°. For case 2, when the primary freestream is smaller, the mixing characteristics are little changed for different angles. The Proper Orthogonal Decomposition (POD) was applied for case 1 and the results showed that the pair of counter-vortices is the main dominant structure flow in the mixing region. The averaged flow fields, turbulent kinetic energy, and unsteady behavior were analyzed and discussed insight in this study.

Keywords: Mixing layer, splitter angle, convective Mach number, LES, POD.

1. Introduction

Mixing flow is an important problem in fluid dynamics. The mixing flow is understood as the region, where two flows with different velocities interact with each other. This type of flow occurs in many practical engineering applications, such as flow behind engines, convective flow in air and under the sea, and flow in active control regions [1]. Although the geometry shape toward the region is simple, complex flow features with high turbulent intensity may occur in the mixing region. These coherent structures are highly modified by Reynolds number, convective Mach number, and disturbance from the wall surface.

In the early investigation of Reynolds number around 1000, the structures of the mixing layer are known as fundamental Kelvin-Helmholtz instability [2]. This structure develops along the wake region. The transition to turbulence occurs at Reynolds numbers of around 104. At higher Reynolds numbers, the flow in the mixing region is totally changed to turbulent, which is characterized by a pair vortex extending and developing downstream. In an averaged sense, a large shear layer is formed around the centerline. The flow downstream of the mixing layer can be also divided into a transition region, which is located near the wall surface, and in a similar region, in which the flow can be described by selected parameters. The recent study investigating the effect of Mach number on the characteristics of the mixing layer was conducted by Kim et al. [3] by experimental techniques. As noted by Kim et al. [3], the Reynolds averaged Navier-Stokes equations cannot provide accurate results of mixing layers due to under-estimation of the Reynolds shear stress. However, available data by Kim et al. provides [3] sufficient good data for further studies. Relating results of previous studies are shown in Table 1.

In the numerical approach, many works have been conducted to understand the flow characteristics of the mixing layer. In those simulations, the large eddy simulation and direct numerical simulation were often applied. A short summarization of the mesh used for those two methods is shown in Table 1. Laizet et al. [4] for example, investigated the effect of a thick splitter plate on the wake structure by applying the DNS. The mesh size in their study was around 29 million cells. Since the DNS was applied, the Reynolds number in their study was less than 700, which prevented the real application. As can be seen the mesh size in those numerical methods is sufficiently large, which consumes high numerical time and prevents the application for a wide range of the model and configurations. A less expensive and highly accurate numerical technique is required for further investigation.

Published online: May 30 2024

Table 1. Summary of mesh size and methods used for studying mixing flow.

Research, Year	Method	Type	Size of Mesh
Doris et al. [5], 2000	LES	3D	1.8M
Sankaran and Menon [6], 2005	LES-LEM	2D	136K
Sharma et al. [7], 2011	LES	3D	98M
Mankbadi et al. [8], 2017	LES	3D	14.4-120M
Liu et al. [9], 2018	LES	3D	11.25M
Konark et al. [10], 2019	LES	3D	5.76M
Cheng and Chen [11], 2021	LES	2D	300K
Laizet et al. [4], 2010	DNS	3D	29M
Zhou et al. [12], 2012	DNS	3D	370M
Qi et al. [13], 2018	DNS	3D	190M
Zhang et al. [1], 2019	DNS	3D	103M
Takamure et al. [14], 2018	DNS	3D	2300M
Shi et al. [15], 2021	DNS	3D	21M
Daotong et al. [16], 2021	DNS	3D	420M

Table 2. Relating previous studies of mixing layers at subsonic flow.

Researchers, Year	Convective Mach number	Flow conditions	Methods	Results
Goebel and Dutton [24], 1991	0.2, 0.46, 0.69, 0.72, 0.86, 0.99	Compressible	Experiments (laser Doppler velocimeter)	In fully developed regions, transverse turbulence intensities and normalized Reynolds stresses decrease with increasing Mc, streamwise turbulence intensities and kinematic Reynolds stress remain constant.
Barre and Bonnet [25], 2015	1.0	Compressible	Experiments (laser Doppler velocimeter)	The structure of the Reynolds stress tensor is not affected by compressibility.
Kim et al. [3], 2019	0.19, 0.38, 0.55, 0.69, 0.88	Compressible flow	Experiments (PIV)	- Peak of the kinematic Reynolds stress decreases with increasing Mc. - Compressibility increases, streamwise normal stress increases, transverse and spanwise decreases, and shear stress remains constant.
Tan et al. [26], 2017	0.2	Weak compressibility	Experiments (PIV)	- In the self-similar region, linear velocity thickness increases at a constant slope of 0.0232.
Zhang et al. [27], 2016	0.2	Compressible flow	-	- Interaction of vortex and shock wave was presented. - Large-scale structure induced by high forcing frequency vibration.
Wang et al. [28], 2013	0.2	Compressible flow	-	- Rectangular lobed mixer. - Large-scale streamwise vortices are accompanied by the development of K-H vortices.

Note that although the supersonic flow of mixing flow is important, the flow under subsonic conditions should be also investigated to understand aerodynamic characteristics. The application of the mixing flow under subsonic conditions could be the flow around the engines of airplanes and unmanned aerial vehicles. A summary of previous studies under subsonic flow is summarized in Table 2, which provides good results for validation of numerical study. Additionally, although many studies were conducted, the mixing layer generated by the non-pressure-gradient wall was focused. Practically, the high adverse pressure gradient may occur near the outlet of engines, which makes the mixing layer much more complicated. Chung [17], for example, studied the effect of convex corners at the upper surface on the pressure distribution on the slant. He indicated that a low-pressure region is formed around the shoulder and it has a large effect on the downstream flow. Zhang et al. [18, 19] investigated the effect of a finite splitter thickness on the large-scale structure of the supersonic mixing layer. They presented that increasing the thickness of the splitter enhances the mixing region and the vortice scale. However, the pressure gradient in their studies is almost zero because the flat plate was used. Estakhrsar et al. [20] investigated the effect of nozzle angle on the mixing layer of the wake. They showed that although the angle has no significant effect on the discharge coefficient, the velocity coefficient and nozzle efficiency have a large change. For the low-speed flow, Tran et al. [21–23] conducted various tests to investigate the effect of slant angle on the surface and wake flow of axisymmetric models. This type of mixing flow can be understood as a typical mixing flow, where the inner velocity is zero. By changing the slant angles, a typical flow with a separation bubble was generated on the slant surface, which has a large effect on the wake structure and drag of the model. It indicates that although the geometry of the splitter plate is simple, a change in its geometry can have a large effect on the mixing layer due to the interaction of near wake and mixing region. Additionally, the flow behavior of the mixing layer is not totally classified at incompressible conditions due to the limitations of the previous studies.

The purpose of the current study is to classify the effect of splitter angles on the characteristics of mixing regions. By changing the angles, the near wake structure will be modified. Consequently, the different size of the wake is generated and its effect on the mixing region is simulated. Additionally, the pressure gradient will occur on the surface and the flow conditions of the current study are quite different from previous studies of the mixing region. The current study focuses on incompressible flow, which occurs usually in nature, such as flow in the sky or under the sea. For that aim, the numerical simulation based on improving the model of RANS and LES is applied. We proposed to use a generalized k-ω (GEKO) model with modified mixing coefficients for simulation. The results of numerical methods are firstly validated by experimental data with the same flow conditions for the case of zero pressure gradient. Then the simulation is applied to various angle configurations. Our results show that the mixing layer has a large effect on the flow. When the slant angle is small and the upper velocity is high, the position of the mixing layer occurs from the leading edge of the splitter. That location moves to the trailing edge with the generation of wake structure around the slant. The mixing length increases with the slant angle in that case. However, the mixing region is less affected when the velocity at the upper surface is selected as a low value. The rest of the paper is organized as follows: section 2 presents the numerical setup and flow conditions; Section 3 presents the results of the current study. In section 4, the unsteady characteristics of the mixing region are discussed. Finally, this study concludes in section 5.

2. Numerical Setup and Validation

2.1. Model geometry and numerical domain

The standard model geometry with a 0° slant angle (flat plate) used in this study has the same dimension as shown by Kim et al. [3] for validation. The upper and lower parts are separated by a thin wall splitter. The numerical domain is shown in Fig. 1. Note that the reversed flow region can occur at outlet flow. Consequently, the numerical region is sufficiently long to capture the wake structure of the mixing layer. Additionally, in two-dimensional flow simulation, the kinetic energy was overpredicted as shown in previous studies [18-19]. Consequently, the three-dimensional flow is required for the simulation. In the current study, the numerical domain has a dimension of 1100 mm × 900 mm × 20 mm, as shown in Fig. 1b. Here, the z direction has a small size to reduce the numerical time in large eddy simulation. Consequently, the current results are two quasi-three-dimensional flows.

To investigate the effect of pressure gradient on the aerodynamic characteristics of mixing layers, a slant surface β is generated as shown in Fig. 1. Here, the length of the slant is fixed at 100 mm, while its angle is changed from 0 to 40°. Additionally, the length of the lower surface of the splitter is also fixed when changing angle β. Since the length of the slant is fixed, it is easier to capture and compare the flow for different angles. The velocity of the two inlets is set to obtain the selected convective Mach number. Here, two cases are considered. In case 1, Inlet 1 (primary freestream) is set at U_1 = 152 m/s while the velocity of inlet 2 (secondary freestream) is U_2 = 35 m/s. In case 2, the velocities of Inlet 1 and 2 are U_1 = 35 m/s, and U_2 = 152 m/s, respectively. The convective Mach number in two cases is the same as M_c = 0.185. The selection of difference velocity allows to investigate the effect of high and low velocities on the wake flow. The convective Mach number is the same as a previous experimental study by Kim et al. [3] for the validation. Additionally, this case corresponds to subsonic application, which is the main focus of the current study. The outlet is considered the pressure outlet. The two surfaces of the splitter are selected as non-slip walls. The front and rear walls are chosen as symmetry while the top and bottom surfaces are selected as the inviscid wall.

Structure mesh with the type of hexahedra types is generated using the Block Mesh function in Open Foam. The initial thickness of the mesh is 6×10^{-6} m with a development of 1.1 for the region of 5% from the wall. In the other region, the ratio of the mesh was 1. A high volume of mesh is generated around the model, the leading and trailing edges of the slant, and near the centerline of the wake region. The maximum skewness of the mesh is 0.02. The structure of the mesh around the model and distribution of y^+ is shown in Fig. 2. The maximum y^+ is around 2, which occurs around the Inlet flow. In the slant surface, the y^+ is smaller than 1, which is sufficient for the simulation. The results of the boundary layer shown in Appendix A also indicate that the boundary layer before the slant can be captured well by the current simulation method.

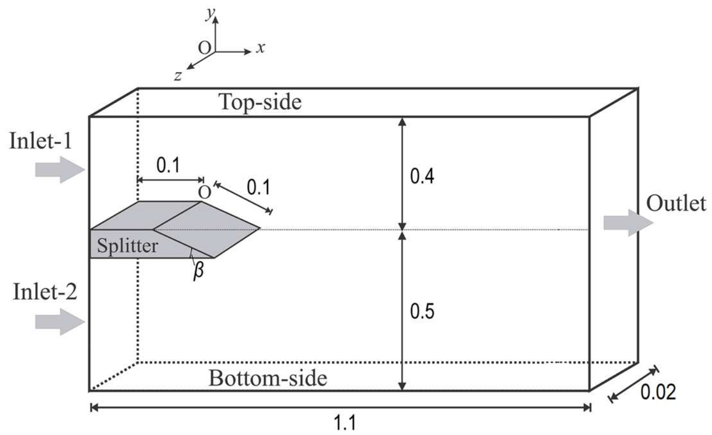

Fig. 1. Model geometry and numerical domain (unit in m).

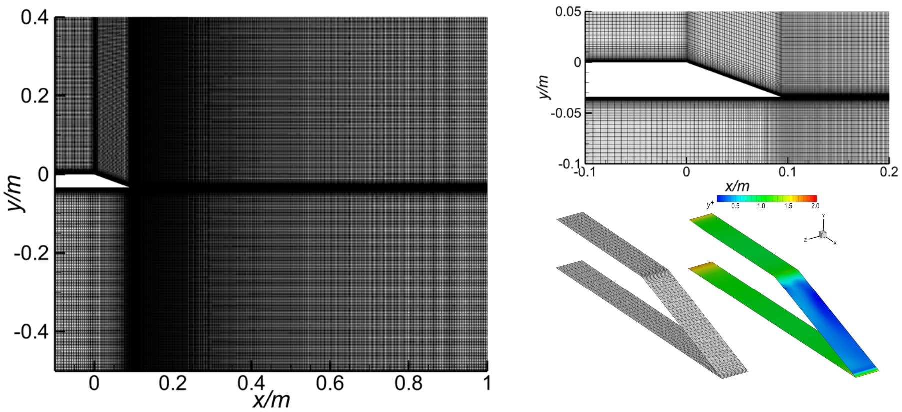

Fig. 2. Mesh structure around the model and distribution of y^+.

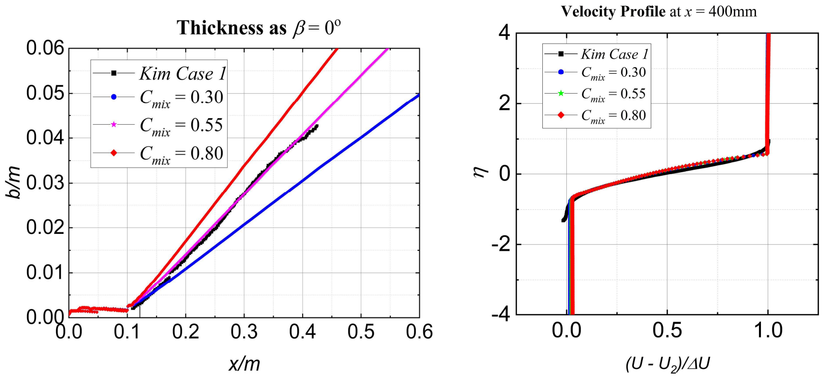

Fig. 3. Effect of C_{mix} on the numerical results.

2.2. Numerical schemes

The selection of numerical schemes is important for the results. For saving numerical time, previous studies often used the Reynolds-averaged Navier-Stokes (RANS) method for simulation wake flow [29, 30]. However, as shown by Kim et al. [3], RANS cannot provide accurate results of the mixing region due to the overestimation of turbulent kinetic energy (TKE) and Reynolds shear stress. Recently, the generalized k-ω (GEKO) model has been presented and shows a high potential in the prediction of turbulent flow characteristics [31, 32]. This is a based k-ω two-equation model, which allows to selection of different coefficients for suitable flow types without other effects on the basic calibration of the model. Based on the method, six parameters can be modified. They are C_{sep} for adjusting the separation, CNW for adjustment of the wall shear stress and wall heat transfer rates, C_{mix} for adjustment of the shear layer flows, C_{jet} for adjustment results of the jet flow, and C_{corner} for adjustment of the secondary flow in corners and C_{curv} for curvature correction. A second-order scheme is selected for the deviation of pressure, velocity, and other turbulent quantities equations. Pressure-velocity coupling (COUPLED) algorithms are selected for RANS simulation. The convergence criterion is set as 10^{-6} for all equations.

This study focuses on the mixing region of the flow, hence the C_{mix} coefficient is adjusted for obtaining the averaged flow fields. As shown in Fig. 3, the coefficient C_{mix} highly modifies the shear layer thickness. Note that increasing C_{mix} leads to the growth of the eddy-viscosity in the free-shear region. Here, b is the shear layer thickness, which is determined by a region of 90% primary velocity at the upper and 90% of the secondary velocity at the bottom. Additionally, m stands for one meter. The mixing layer transverse similarity coordinate η is determined as $\eta = (y - y_0)/b$, where y_0 is the local shear layer midpoint. By changing the C_{mix}, the shear layer thickness is highly modified. At the mixing coefficient of $C_{mix} = 0.55$, the results of shear layer thickness are high agreement with experimental data by Kim et al. [3]. In contrast, the coefficient η changes little by the selection of C_{mix}. For obtaining good results of mixing layer in RANS, the coefficient of $C_{mix} = 0.55$ is selected for all simulation cases. Other parameters are selected as defaulted. Since the incoming flow, numerical setup and meshing generation methods are the same for different splitter angles, it is expected that the difference of the results should be from the effect of the geometry. Additionally, changing C_{mix} may lead to problems due to lacking experimental data for the validation.

To obtain the behavior of unsteady flow, the large eddy simulation (LES) with sub-grid scale model WMLES was also conducted. The equations of the wall function WMLES have below forms for momentum, energy, and eddy-viscosity equations [33]:

$$
\begin{gathered}
\frac{d}{dy}\left[\left(\mu_{wm}+\mu_{t,wm}\right)\frac{dU_{wm}}{dy}\right]=0 \\
\frac{d}{dy}\left[c_p\left(\frac{\mu_{wm}}{\Pr}+\frac{\mu_{t,wm}}{\Pr_{t,wm}}\right)\frac{dT_{wm}}{dy}\right]=-\frac{d}{dy}\left[\left(\mu_{wm}+\mu_{t,wm}\right)U_{wm}\frac{dU_{wm}}{dy}\right] \\
\mu_{t,wm}=\kappa\rho_{wm}\sqrt{\frac{\tau_{w,wm}}{\rho_{wm}}}y\left[1-\exp\left(-y^*/A^+\right)\right]^2 \\
y^*=\frac{y\sqrt{\rho\tau_w}}{\mu}
\end{gathered}
\tag{1}
$$

The constant parameters are selected as $\kappa = 0.41$, $A^+ = 17$, and $\Pr_{t,wm} = 0.9$.

However, since the large eddy simulation requires a long simulation time, only three typical angles are selected for the calculation. To reduce the numerical time, the RANS results serve as the initial values for the LES. In LES, the step time was fixed at 4e-6 s, which provides a maximum Courant number of 2. Similar to RANS simulation, second-order accurate derivatives of numerical parameters are selected for the simulation. The second-order implicit is chosen for the transient formulation. The PISO scheme is employed for the velocity and pressure fields. The simulation was conducted over 0.003s. The simulations for each case were calculated over three weeks. The results are saved after 10 steps for data processing. Both RANS and LES were conducted by Ansys Fluent software. The program is copyrighted by Le Quy Don Technical University, Vietnam. The post-data processing was conducted using MATLAB codes, which were written by us. Detailed numerical cases and schemes are presented in Table 3.

2.3. Effect of mesh size on the results

Figure 4 presents the effect of mesh size on the thickness and of the mixing layer by RANS simulation. As can be seen, the thickness and velocity profile changes little for different mesh sizes. It can be explained that the results of the current study are not sensitive to the mesh. For balance between the numerical time and the results, the mesh with a size of around 1.2 million cells is selected for the numerical process. Note that in comparison to previous studies shown in Table 1, the size of the current study is much smaller. However, the results are consistent well to the experimental data. The selection of the simulation model and adjustment of the numerical parameters are important for the results.

Table 3. Numerical scheme selection.

Splitter angle (°)	RANS 3D, GEKO	LES 3D
0	×	×
5	×	
10	×	
15	×	×
18	×	
20	×	×
25	×	
30	×	
40	×	

2.4. Streamwise velocity at zero splitter angles

In this section, we compare the averaged streamwise velocity by the experimental and numerical simulation for the case of the flat splitter to examine the results. As can be seen in Fig. 5, the results of the two methods show a similar pattern with a generation of mixing layers around the center of the plate, where the velocity changes from the secondary freestream at the bottom to the primary velocity at the upper part. The generation of those velocity structures is from the fact that the three-dimensional structures of the vortices roll up and widen downstream in mixing regions. Note that for the average flow, RANS probably provides more accurate results in comparison to LES. The reason is because of the LES requires higher mesh quality and a small time-step. In the RANS simulation, a wall function is used. As a result, the mesh quality, and mesh aspect ratio can be rougher. For a better understanding of the structure, the comparison of thickness can be compared as shown in Fig. 3.

Figure 6 presents the comparison of mean magnitude velocity profiles at different stations along the mixing region. The results from both simulation and experiments present that the shear layer at the below part grows faster than the upper surface. Note that although plotting in a plane, both experimental and simulation data used three-dimensional velocity components. The two-dimensional flow, which was not shown here, provides an overestimation of the velocity. Consequently, the two-dimensional flow simulation can bring insufficiently accurate results, as was also noted in the previous studies.

Various data for validation of the results for the flat splitter plate have been presented. The current study illustrates that the results of RANS and LES are highly in agreement with previous experimental results. Consequently, the current numerical methods are then applied for the splitter with angles for understanding the relation between the flow characteristics of the mixing region and the geometry of the plates.

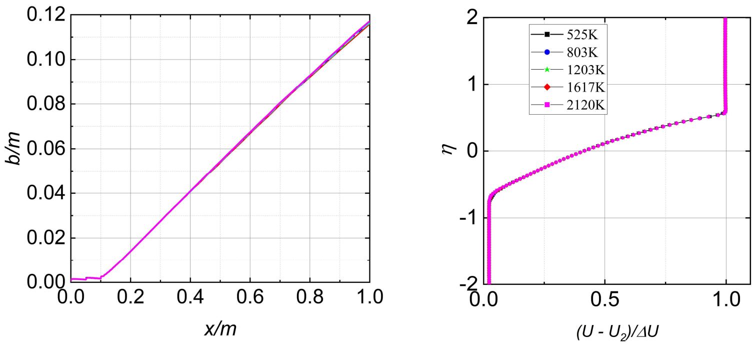

Fig. 4. Effect of mesh size on the shear layer thickness and mixing layer transverse similarity coordinate.

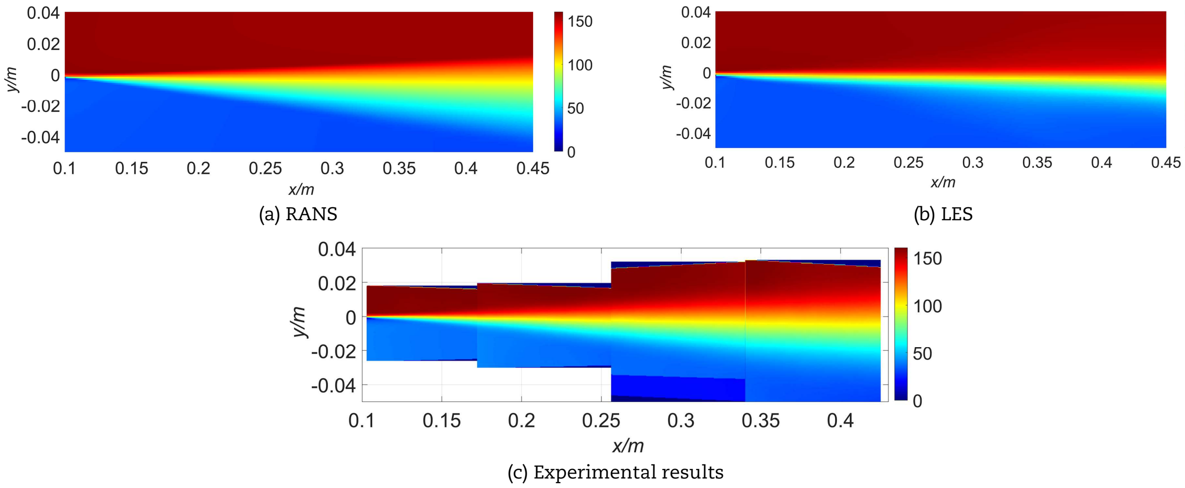

Fig. 5. Comparison of the streamwise velocity between numerical and experimental methods.

3. Results and Discussions

3.1. Averaged velocity fields

Figure 7 shows the averaged streamwise velocity on the symmetric plane z = 0 for different splitter angles by the RANS GEKO method. The velocity scale on the color contours ranges from -35 m/s to 205 m/s for all cases. Note that since the velocity changes around the splitter edges, the color contour in this section differs from section 2.4. Generally, a mixing region is generated around the line y = 0, which is characterized by a change in the velocity from U_2 to U_1. The effect of splitter angles mainly occurs on the upper surface, where the geometry is highly modified with a generation of non-pressure gradients. A slight increase of the velocity is observed at the leading edge of the splitter and results in the modification of the mixing region. Interestingly, the mixing positions change from the trailing edge of the splitter for the angle below 20° to the leading edge for the angle above 20°, where a low-velocity region is observed around the splitter slant surface.

For comparison of the shear layer, Fig. 8 presents the development of the shear layer for different splitter angles. The experimental results of the flat splitter by Kim et al. [3] were also noted for comparison. At a fixed horizontal position, the shear layer region widens with increasing splitter angle up to 18°, then it reduces and remains at a similar value for higher angles. Note that although much data was added, a perfectly linear increasing the shear layer for all cases. The difference in the shear-layer gradient is summarized later in Fig. 16. A slight curve contour was observed at $x/m < 0.1$ for the angles above 10°. It is explained by the effect of the wake structure (shown later in Fig. 9), which is generated on the slant and has a large effect on the downstream flow. At $x/m > 0.1$, a linear increase in the shear-layer thickness is observed for all configurations. Interestingly, the normalized growth rate (db/dx) remains at a similar value for different angles for $x/m > 0.1$.

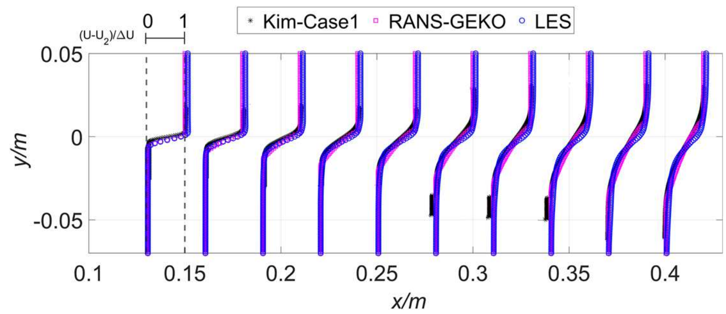

Fig. 6. Comparison of the velocity profiles and TKE between numerical and experimental results.

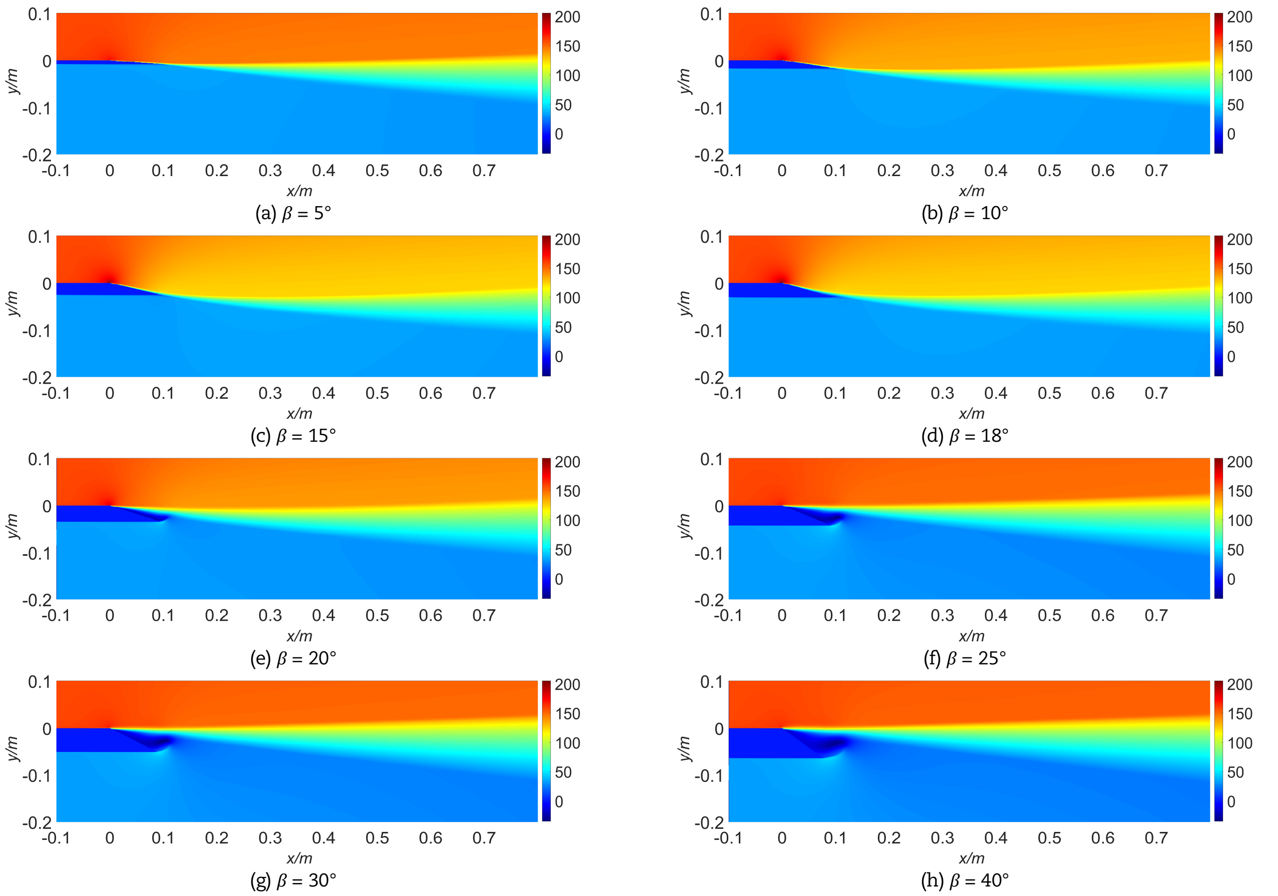

Fig. 7. Averaged flow fields for different slant angles.

3.2. Wake structure near the splitter

For details of wake structure and understanding its effect on the mixing region, a zoom-in streamline mixing with streamwise velocity near the splitter plates is presented for different angles (Fig. 9). Some modifications of the flow close to the surface are witnessed for changing angles. In detail, when the angle is small, the flow is smooth and the mixing layer occurs from the trailing edge of the splitter. At the slant angle of 20°, a wake is generated on the slant with a recirculation and low-velocity region inside. This wake structure becomes broadening with increasing slant angles. For the angle of 40°, for example, the near wake is featured by two counter-rotating vortices, beginning from the upper and lower edges. The wake results in moving backward from the mixing position to the leading edges. For a higher slant angle, two recirculation wakes are formed behind the slant and the mixing layer remains similar in the case of 20°.

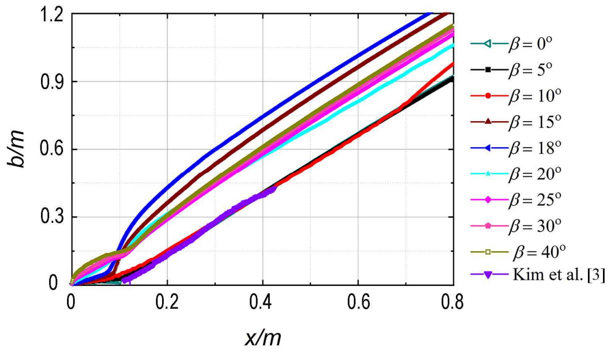

Fig. 8. The development of shear-layer thickness for different slant angles in case 1.

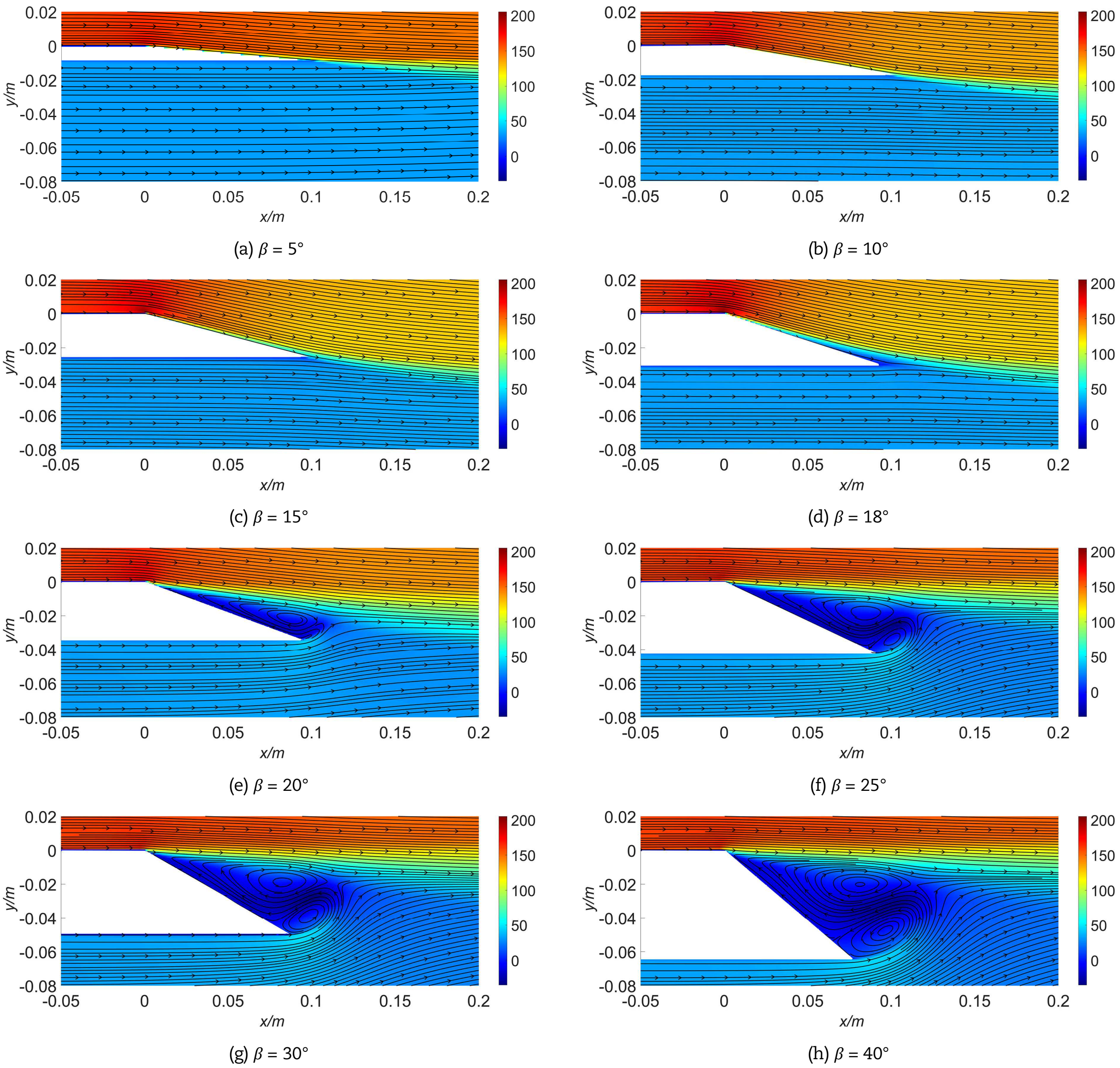

Fig. 9. Near wake structure and streamlines above the slant of the splitter.

3.3. Surface skin friction and pressure distributions

For the details of the flow on the slant, Fig. 10 presents the streamwise skin-friction values for different angles. The formula for calculating the skin friction is shown in Eq. (2). The skin-friction values allow to analyze the separation and reattachment positions on the surface, which helps analyze the flow behavior. Here, the separated region is featured by negative skin friction values. For slant angles above 18°, skin friction on the slant is negative, which indicates that the flow is fully separated at the leading edge. The results are similar to previous observation by Estakhrsar et al. [20] for the supersonic flow on the slant. It should be noted that the flow with a separation bubble on the slant, which was reported in previous studies for axisymmetric boattail and Ahmed body, was not generated for the slant angle between 12 and 18°. It is because the effect of two upstream velocities is quite strong, which prevents the development of complicated flow on the surface. The effect of the near wake on the mixing layer occurs at just x/m < 0.1, which results in a change in the linear curve of the shear-layer thickness, as shown in Fig. 6. At x/m > 0.1, the wake flow has only effect on the width of the shear layer thickness while the gradient of the shear-layer thickness remains near constants.

$$C_f = \frac{\tau_{wx}}{\frac{1}{2}\rho_\infty U_C^2} \tag{2}$$

where ρ_∞ is the air density, $U_c = ½(U_1 + U_2)$ is the average velocity and τ_{wx} is shear stress in the slant surface of the splitter. Here, U_1 and U_2 are the primary and secondary velocities, respectively.

The pressure distribution on the slant surface at plane z = 0 is shown in Fig. 11 for both the upper and lower surfaces of the splitter. The pressure coefficient is calculated by Eq. (3). Since the lower surface is flat, the pressure remains at the same value at around 0. Due to the change in geometry of the upper surface, low pressure with a peak at the leading edge is generated. The peak of pressure becomes lower for increasing slant angle up to 18°, where the flow is in the vicinity of the full separation. The low pressure near the edge for that case results in an increasing velocity around the shoulder, as shown in Fig. 7. The fully separated flow results in the drop of the pressure around the leading edge, which can be understood as the result of the wake flow region. The trend of pressure around the shoulder for different slant angles is consistent with previous observations by Tran et al. [23] for axisymmetric boattail flow. The generation of low pressure has a large effect on near-wake structure as well as the flow of the mixing region.

$$C_p = \frac{p}{\frac{1}{2}\rho_\infty U_C^2} \tag{3}$$

where p is the pressure value on the wall of the splitter.

3.4. Turbulent kinetic energy characteristics

Figure 12 summarizes the three components of the TKE for different slant angles tested. The experimental results by Kim et al. were also added for the plate splitter. The high values of TKE occur around the centerline y = 0. For the baseline case, the maximum TKE reaches 4% of the different velocities $\Delta U = U_1 - U_2$, which is similar to the previous experimental study. A similar result is observed for that case of 5°. Increasing the angle further, the TKE slightly decreases to angles up to 18°, then it increases again. In the case of fully separated flow, the TKE above the slant is sufficiently high, which is a result of the interaction of the mixing region and near-wake flow.

3.5. Characteristics of the mixing flow in case 2

The effect of splitter angles on the mixing flow was investigated for case 1 when the primary velocity at the upper part was high. However, due to the application, the geometry of the model can be changed. Consequently, to answer the question about the impact of the angle on the flow characteristics of the mixing layer, further study, which is named case 2, is conducted. In this case, the velocity at the upper inlet was set as a low value, while the bellow inlet was a high value. Here, this study first focuses on steady behavior. Consequently, RANS simulation, which was set up the same as it was shown in section 2, is applied and only velocities are changed. The results of the mixing layer for different slant angles are presented in Fig. 13. The present results indicate that the location of mixing positions remains at a trailing edge of the slant. Additionally, the full separation positions occur only for slant angles above 20° and the wake becomes larger with increasing the slant angle and thickness of the slant. However, the pattern of the wake changes significantly in comparison to case 1. The length of the transition region, which is shown later in Fig. 17, is less affected by the slant angle. It is suggested to build engine models with a convex cavity outside to prevent the change of the mixing flow in the wake region. Note that the results of the current study were not presented in previous observations for mixing regions. Note that previous studies mainly focused on the Mach number, and numerical scheme, while the geometry of the splitter plate was little changed.

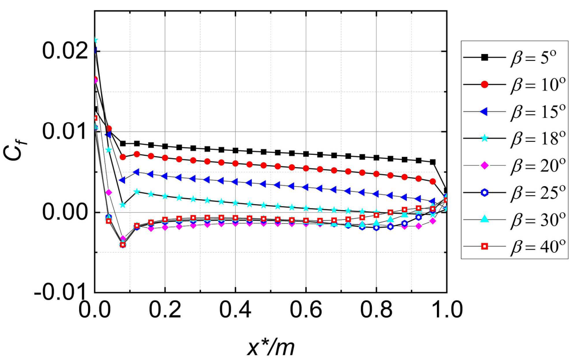

Fig. 10. Streamwise skin friction on the upper surfaces of the splitter.

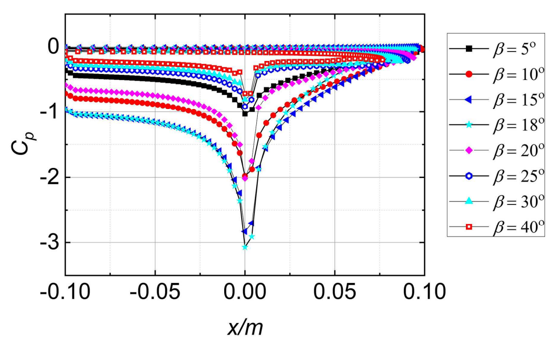

Fig. 11. Pressure distribution on the symmetric surface of the splitter.

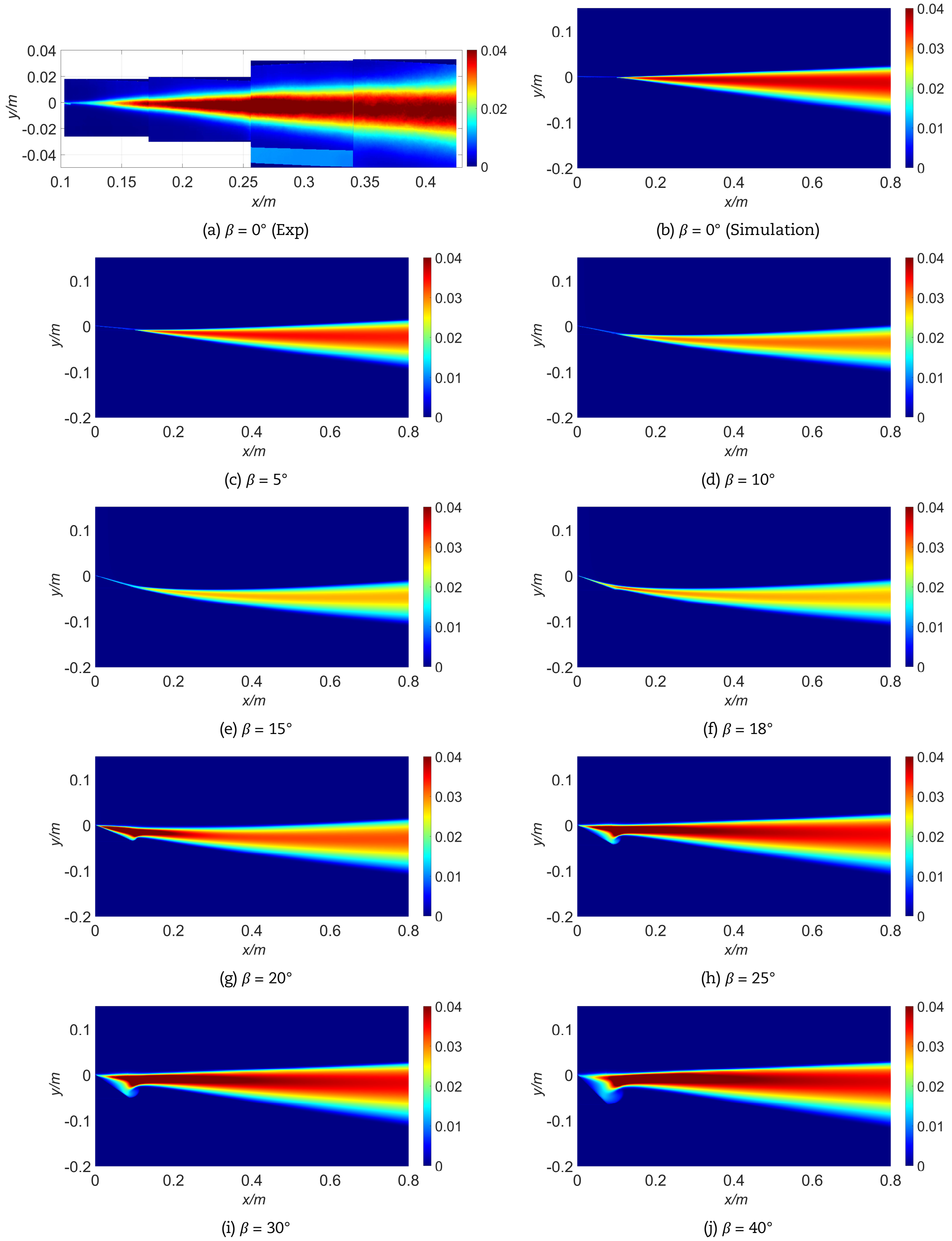

(a) β = 0° (Exp)　(b) β = 0° (Simulation)

(c) β = 5°　(d) β = 10°

(e) β = 15°　(f) β = 18°

(g) β = 20°　(h) β = 25°

(i) β = 30°　(j) β = 40°

Fig. 12. TKE for different slant angle.

Figure 15 presents the shear-layer thickness for case 2, where the below velocity is high. As can be seen, the thickness slightly increases with slant angle. Hence the effect of splitter shape on the mixing characteristics is quite low for those configurations. The effect of flow velocity at the lower part on the upper surface can be clearly identified from the results of the separation on the surface, as shown in Fig. 14. As can be seen although the velocity at the upper surface for case 1 is large than case 2, the fully separated flow occurs at lower slant angle (of 20°) for case 1, in comparison to an angle of 25° for case 2. The effect of the velocity on the separation flow is different from the single flow type on the axisymmetric boattail model, where separation flow occurs at the lower slant angles when the velocity is higher.

3.6. Gradient of shear layer and length of mixing region

Figure 16 summarizes the gradient of the shear-layer thickness in the similarity region and the length of the transition region by ratio with the shear-layer thickness. As can be seen the gradient of the shear-layer thickness for case 1 slightly increases for angle up to 18°, then it decreases for fully separated flow. For case 2, the gradient of the shear-layer thickness remains nearly at a constant value of 0.13.

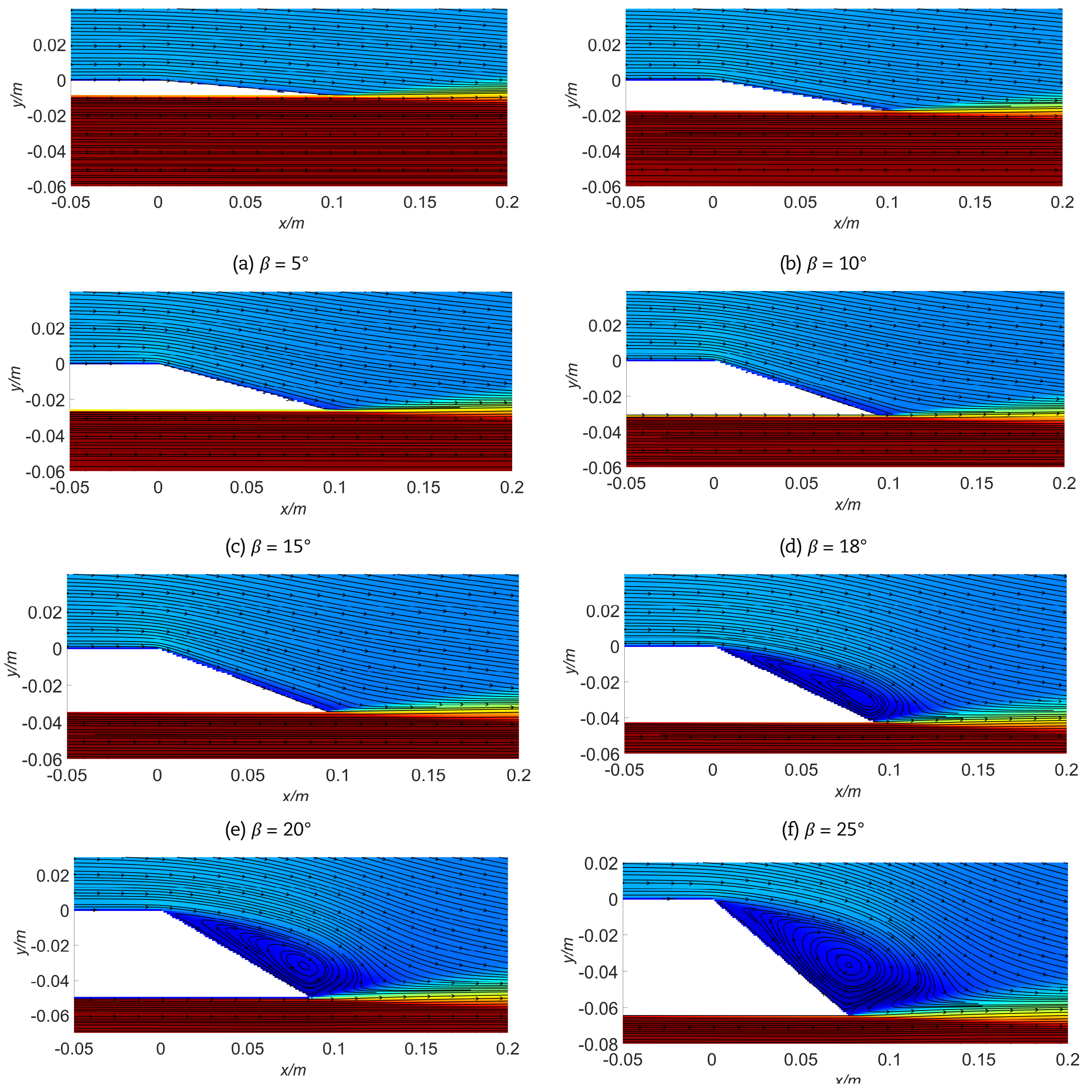

(a) $\beta = 5°$ (b) $\beta = 10°$

(c) $\beta = 15°$ (d) $\beta = 18°$

(e) $\beta = 20°$ (f) $\beta = 25°$

(g) $\beta = 30°$ (h) $\beta = 40°$

Fig. 14. Near wake structure and streamlines above the slant of the splitter for case 2 (Inlet 1 is set a low velocity, while Inlet 2 is high).

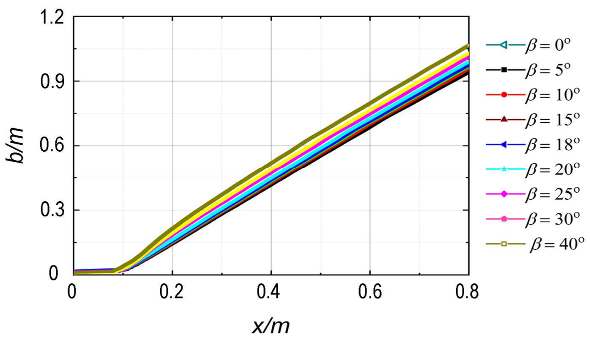

Fig. 15. The development of shear-layer thickness for different slant angles in case 2.

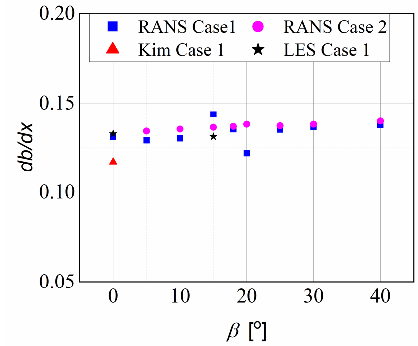

Fig. 16. The variation of the shear-layer thickness gradient.

The length of the mixing region is very important for the practical application. For example, the mixing region is required as short as possible for the region inside the engine to increase its performance. However, for the mixing flow behind the engine, the long mixing region is a problem for noise and instability. From the literature reviews, the length of the mixing layer is determined by the region from the edge of the splitter plate to a position where the shear layer thickness linear develops or to a position, where the Reynolds shear stress becomes constant. However, using the mixing layer, it is very difficult to determine the length of the transition region as shown in previous studies by Zhang et al. [34]. Based on the determination of the similarity region, we proposed a new method for obtaining the length of the mixing region. For the details, the mixing layer transverse similarity coordinate is determined. The mean similarity profiles near the outlet, where flow is consumed as the similarity region, are calculated. The root mean square at each vertical position along the streamwise direction is calculated. The length of the transition region is determined by the region, where the root square is higher than 1.5%. Note that although the determination is simple, it was not presented in previous studies. We summarize the length of the transition region in Fig. 17. As can be seen, the length of the mixing region remains nearly constant for angles below 20 at 0.3 m. Then, it linearly increases with splitter angles due to the generation of full separation on the slant. When the primary velocity is higher, the length of the mixing region is higher than in the case of low primary velocity.

3.7. Proper Orthogonal Decomposition analysis

In this section, Proper Orthogonal Decomposition (POD) analysis is applied to obtain the most dominant modes of flow in the mixing region. The initial proposal of the POD was made by Berkooz et al. [35] for the study of fluid flow, and it has been widely utilized in previous research, specifically for Particle Image Velocimetry (PIV) measurements. The fundamental principle underlying POD is its ability to separate modes within the flow. Although a single POD mode encompasses a broad spectrum of frequencies, it facilitates the reconstruction of flow modes in descending order of energy. Consequently, the initial modes effectively capture the primary mechanisms governing the flow. In this section, our emphasis lies on examining the primary flow patterns rather than individual frequencies, and we will employ the POD technique for this purpose. In the POD analysis, the velocity fields at time "t" are decomposed into mean and fluctuation components, as below equations:

$$\boldsymbol{u}(x,t) = \bar{\boldsymbol{u}}(x,t) + \boldsymbol{u}'(x,t) \tag{4}$$

The fluctuation elements $\boldsymbol{u}'(x,t)$, which contain both two velocity components u, v can be expressed as a combination of temporal scalar coefficients $a_k(t)$ and orthogonal spatially independent function $\varphi_k(x)$ as below:

$$\boldsymbol{u}'(x,t) = \sum_{k=1}^{\infty} a_k(t)\varphi_k(x) \tag{5}$$

The functions $\varphi_k(x)$ contain eigenmodes or POD modes of the flow while the coefficients $a_k(t)$ show time-scale characteristics of the model. The function $\varphi_k(x)$ can be calculated from the Singular Value Decomposition (SVD) of the matrix A as below:

$$A = \begin{bmatrix} u_1'^1 & u_1'^2 & \dots & u_1'^N \\ \vdots & \vdots & \vdots & \vdots \\ u_M'^1 & u_M'^2 & \cdots & u_M'^N \\ v_1'^1 & v_1'^2 & \cdots & v_1'^N \\ \vdots & \vdots & \vdots & \vdots \\ v_M'^1 & v_M'^2 & \cdots & v_M'^N \end{bmatrix} \tag{6}$$

where N is the number of the snapshot and M is the total element of each velocity component. In this study, we propose to use POD for velocity fields from LES to obtain the most important features of the mixing layer with different slant angles. A region of $0.10 < x/m < 0.45$ in the horizontal direction and $-0.06 < y/m < 0.04$ in the vertical direction is selected for POD analysis. This region shows the most change in the flow behavior of the transition flow. The dataset for POD process contains over 2000 samples for each case.

The spatial distribution of the first five POD modes is shown in Fig. 18 for three angles of 0, 15° and 20°. For the flat plate, the large-scale feature of the mixing layer is characterized by a pair of vortices developing along the streamwise direction, which can be seen from the first POD mode. The center of the vortices is slightly changed along the centerline. The similarity of the three modes indicates that this structure is the main feature of the mixing region. The results confirm that the two counterclockwise vortices are the dominant modes of the mixing layer under supersonic conditions The current results indicate that the horizontal distance between two vortexes is around 65 mm in the transition region, which is consistent with previous experimental results by Kim et al. [37] The results are also consistent to previous results by Laizet et al. [9], where the wake is most dominant in the first part of the flow while the existence of the mixing region is clearly identified in the far wake region. For the higher modes, the distance between pair vortexes decreases, which indicates smaller vortex structures. Similar patterns of the spatial modes are witnessed for the splitter with a slant angle of 15°. However, the distance between vortices in a pair is much shorter than in the case of 0°. It can be explained by the effect of sharp geometry at the leading edge of the slant, which increases the pressure peak and reduces the velocity in the wake region. As the results, the turbulent kinetic energy and large-scale structures decrease as shown in Fig. 12. The results of the current study confirm that although the gradient of the shear layer remains constant, increasing slant angles until the generation of full separation flow allows to reduce the length of the transition region and large-scale structure. This outcome is helpful for designing outer mixing flow, which reduces the influence of the mixing region.

Interestingly, the POD modes of the angle of 20° change much in comparison to the two other cases. In detail, the center of the vortex pair is not in the horizontal axis, but at the upper and lower part for the first three modes. Additionally, the distance between the vortex centers rises in comparison to other cases. It can be explained by the effect of the near wake structure on the unsteady behavior of the mixing region. In the details, the existence of the wake on the slant leads to the generation of low-velocity regions in the mixing region, as shown in Fig. 9. As the results, the shear layer develops, turbulent intensity becomes high the flow is more chaotic, and no clear pattern of POD is illustrated.

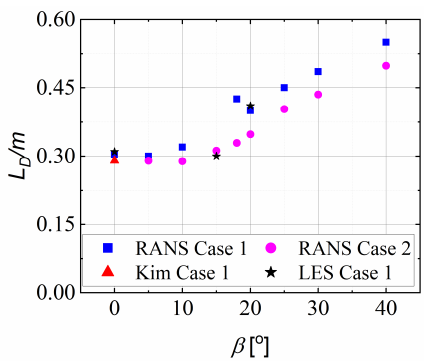

Fig. 17. Length of mixing region as function of splitter angles.

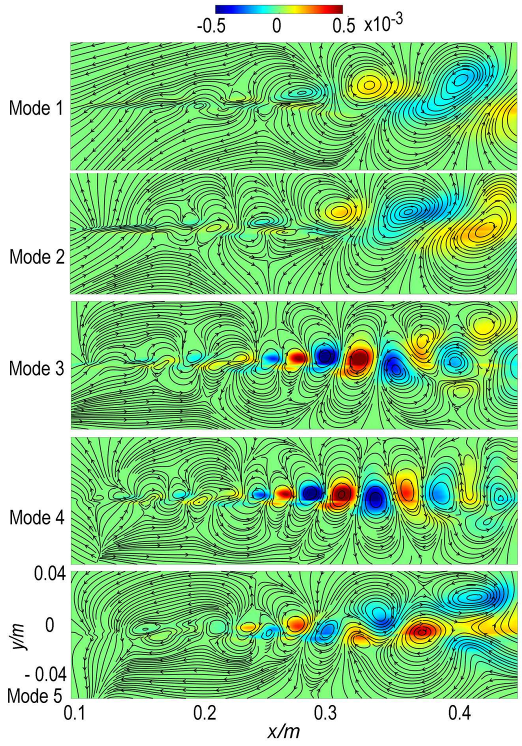

(a) $\beta = 0°$

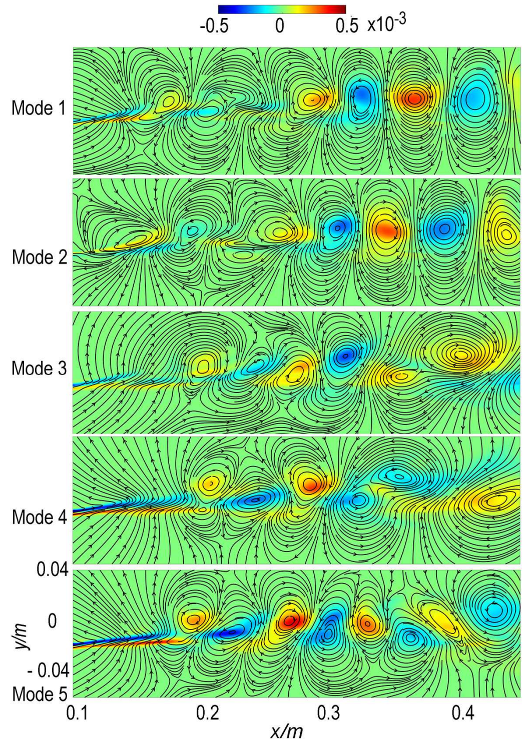

(b) $\beta = 15°$

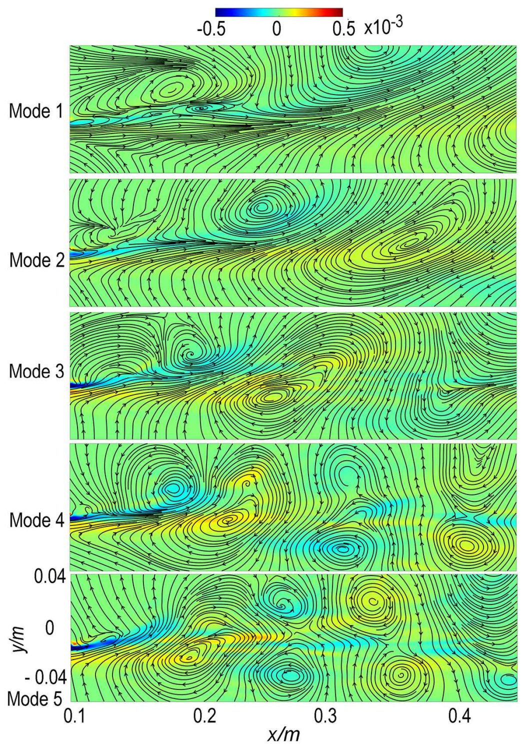

(c) $\beta = 20°$

Fig. 18. The pattern of the first five POD for three angles of 0, 15 and 20°.

The results of fast Fourier transform analysis for the time history of the POD modes for three angles are presented in Fig. 19. Similarity results are noticed for two angles of 0° and 15° with a dominant frequency of around 2000 Hz. Notably, this frequency is not generated for the angle of 20°, where a lower dominant frequency of 500 Hz was observed. The magnitude of power spectra density shows a remarkable decrease for high slant angles. The difference in the observation frequencies for angle 20° in comparison to other cases is probably due to the change of the flow above the slant. Note that the dominant frequency of mixing flow was not paid attention in previous studies of mixing flow.

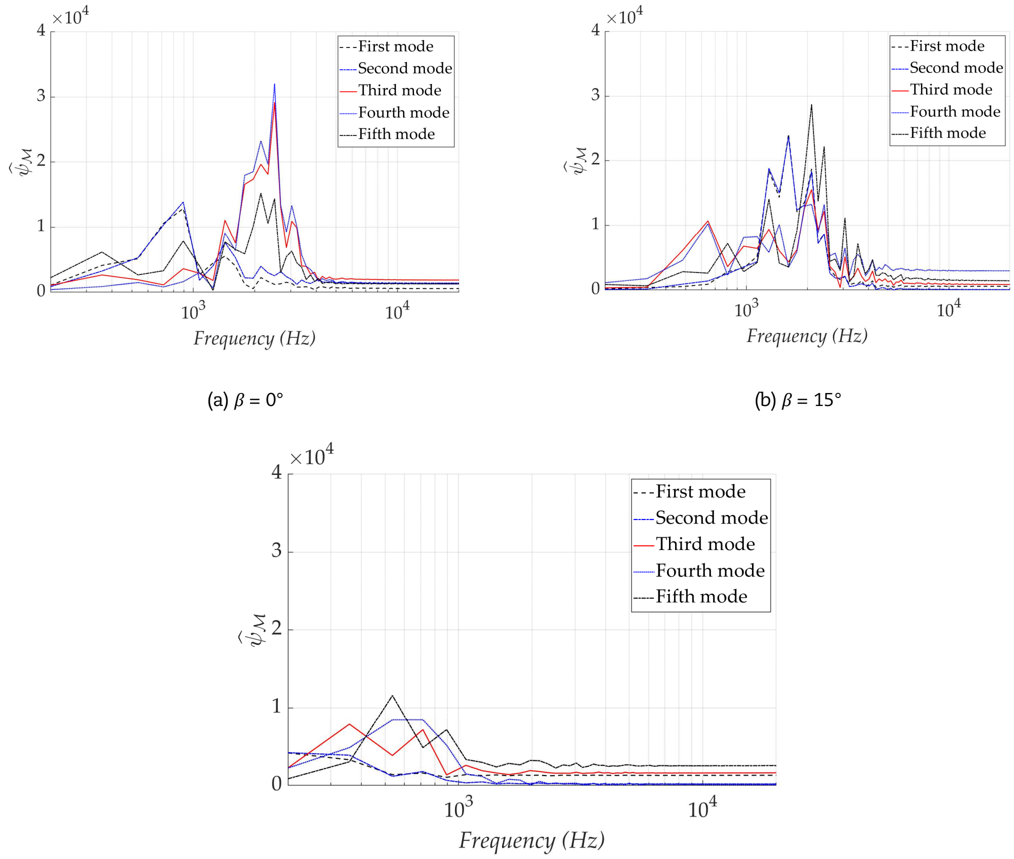

(a) $\beta = 0°$ (b) $\beta = 15°$

(c) $\beta = 20°$

Fig. 19. Frequencies characteristics from the time history of the POD modes.

4. Conclusions

In this study, the effect of splitter shape on flow in the mixing region was investigated by numerical approach. The GEKO turbulent models and large eddy simulation were applied for steady and transition flows. When the numerical coefficients are carefully selected GEKO turbulent model provides sufficiently accurate results of averaged mixing flow in comparison to experimental data and it could be used for further study of the mixing layer to save numerical time. The main contribution of this study is as below.

In case 1, when the primary velocity is high, increasing the thickness and angle of the plate has resulted in the formalization of the wake recirculation region. The flow on the slant becomes full separation at the splitter angle of 20°, and the mixing positions move to the leading edge. The wake structure is highly modified but mixing positions remain at the trailing edge when the primary velocity is set low in case 2. The effect of angle and thickness of the splitter has little effect on the characteristics of the mixing region in that case. A transition of the flow with a separation bubble on the slant, which was reported for axisymmetric boattail flow and flow on the slant surface of Ahmed body, was not generated for mixing flow.

The gradient of the shear layer remains nearly constant at around $db/dx = 0.13$ for two cases. The effect of wake on mixing flow can be found at $x/m < 0.1$ where non-linear development of the shear layer is generated. At the flow is attached to the splitter surface ($\beta < 20°$) the length of the mixing region remains nearly a constant value. When the separation flow occurs, the length of the mixing region increases linearly with the splitter angle. The growth of mixing length is higher for case 1 in comparison to case 2.

The mixing coefficient of C_{mix} in the GEKO model of 0.55 provides the best results. The steady characteristics of the mixing region are seemingly less sensitive to the mesh size of the numerical domain.

In terms of unsteady characteristics, the POD analysis shows that a pair counter vortex is the most dominant mode of the mixing flow. This mode is highly modified for full separation flow on the slant. The time history of POD modes shows a dominant frequency of around 2000 Hz for two splitter angles of 0 and 15°. This frequency reduces to 500 Hz for the splitter angle of 20°.

The results of the current study suggest for a good design of jet engines, the splitter angle should be below 20°. However, detailed results relating to the engines were not presented and there is a task for our further study.

Appendix A

Figure A1 compares the boundary layer profiles of the simulations and experimental results by Kim et al. [3] at 0.005 mm before the splitter for the lower and upper surfaces of Case 1. Due to the limitation of the hot-wire anemometry, the initial positions of the measurement are around y = 1 mm. As can be seen both simulation methods by RANS and LES show close results to experimental data. However, due to the high mesh number, clear information is obtained near the wall. The boundary layer at the lower surface is much thicker than that of the upper surface, which is due to the lower velocity of the Inlet flow. The H-factor is around 1.4, confirming that the boundary layer changes to fully turbulent before the mixing region.

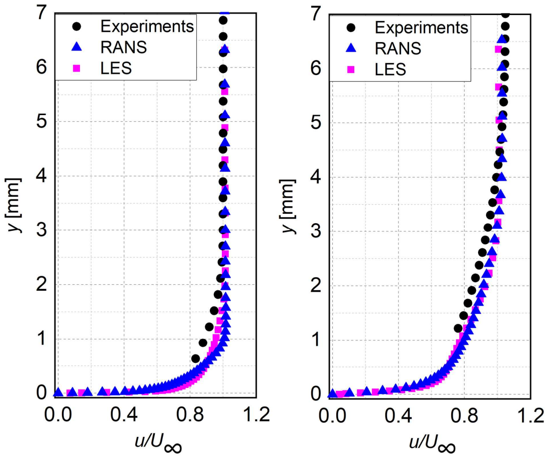

(a) Upper surface (b) Lower surface

Fig. A1. Comparison of the boundary layer profiles.

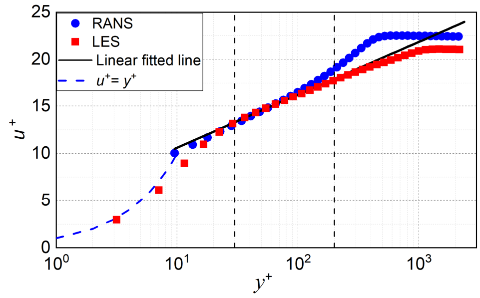

Fig. A2. Boundary-layer profile in the log-law region.

For detailed information on the boundary layer, Fig. A2 presents the log-law region of the boundary layer for the upper surface shown in Fig. A1. Here, u^+ and y^+ present non-dimensional of the velocity and the distance y to the wall. The formula for those parameters is shown as:

$$u^+ = \frac{1}{\kappa}\ln y^+ + C^+ \qquad \text{with} \qquad u^+ = \frac{u}{u_\tau} \;,\; u_\tau = \sqrt{\frac{\tau_w}{\rho}} \;\text{ and }\; y^+ = \frac{yu_\tau}{\nu} \tag{A.1}$$

Here, τ_w is the wall shear stress, ρ is the air density, is u_τ the shear velocity, and is ν the kinematic viscosity. The constant parameters κ and C are selected as $\kappa = 0.41$ and $C^+ = 5.0$.

A function ODE45 is used to find the linear fitted line in the log-law region. Note that due to the limitation of the measurement points near the surface, the experimental data is not used for building the fitted line. As can be seen, the results of the two simulations are close. Additionally, the LES provides more detailed results in the viscous sublayer region ($y^+ < 10$) and the minimum value y^+ can be captured around 3. The results confirm that the first node of the mesh is inside the viscous layer.

Author Contributions

T.D. Nguyen planned the scheme, initiated the project, conducted the simulation, and analyzed the empirical results; D.A. Le suggested the simulations and analyzed the empirical results; V.M. Do suggested the simulations and analyzed the empirical results; A.T. Nguyen developed the mathematical modeling and examined the theory validation; T.H. Tran planned the scheme, initiated the project, and suggested the simulations. The manuscript was written through the contribution of all authors. All authors discussed the results, and reviewed, and approved the final version of the manuscript.

Acknowledgments

We would like thank to Le Quy Don Technical University, Hanoi, Vietnam for supporting this work.

Conflict of Interest

The authors declared no potential conflicts of interest concerning the research, authorship, and publication of this article.

Funding

This research is funded by Le Quy Don Technical University under grant number 23.1.37.

Data Availability Statements

The datasets generated and/or analyzed during the current study are available from the corresponding author on reasonable request.

Nomenclature

b	Shear-layer thickness [mm]	Mc	Convective Mach number
C_p	Skin pressure coefficient	U_1	Velocity of the primary stream [m/s]
C_f	Skin friction coefficient	U_C	Average velocity [m/s]
L_D	Length of mixing region [mm]	β	The slant angle [°]
U_2	Velocity of the secondary stream [m/s]		

References

[1] Tan, J., Zhang, D., Lv, L., A review on enhanced mixing methods in supersonic mixing layer flows, *Acta Astronautica*, 152, 2018, 310–324.
[2] Brown, G.L., Roshko, A., On density effects and large structure in turbulent mixing layers, *Journal of Fluid Mechanics*, 64, 1974, 775–816.
[3] Kim, K.U., Elliott, G.S., Dutton, J.C., Three-dimensional experimental study of compressibility effects on turbulent free shear layers, *AIAA Journal*, 58, 2020, 133–147.
[4] Laizet, S., Lardeau, S., Lamballais, E., Direct numerical simulation of a mixing layer downstream a thick splitter plate, *Physics of Fluids*, 22, 2010, 015104.
[5] Doris, L., Tenaud, C., Ta Phuoc, L., LES of spatially developing 3D compressible mixing layer, *Comptes Rendus de l'Académie des Sciences-Series IIB–Mechanics*, 328(7), 2000, 567–573.
[6] Sankaran, V., Menon, S., LES of scalar mixing in supersonic mixing layers, *Proceedings of the Combustion Institute*, 30, 2005, 2835–2842.
[7] Sharma, A., Bhaskaran, R., Lele, K., Large-eddy simulation of supersonic turbulent mixing layers downstream of a splitter plate, *49th AIAA Aerospace Sciences Meeting Including the New Horizons Forum and Aerospace Exposition*, 2011.
[8] Mankbadi, M.R., Debonis, J.R., Georgiadis, N.J., Large-Eddy Simulation of a Compressible Mixing Layer and the Significance of Inflow Turbulence, *55th AIAA Aerospace Sciences Meeting*, Grapevine, Texas, 2017.
[9] Yang, L., Ben-shuai, F., Chen-xi, Z., Large Eddy Simulation on Development and Evolution of Subsonic-Supersonic Shear Mixing Layer, *ICCFD10 Proceedings*, 2018.
[10] Arora, K., Chakravarthy, K., Chakraborty, D., Large eddy simulation of supersonic, compressible, turbulent mixing layers, *Aerospace Science and Technology*, 86, 2019, 592–598.
[11] Cheng, Y., Chen, Q., Large Eddy Simulation and Dynamic Mode Decomposition of Turbulent Mixing Layers, *Applied Sciences*, 11, 2021, 12127.
[12] Zhou, Q., He, F., Shen, M.Y., Direct numerical simulation of a spatially developing compressible plane mixing layer : flow structures and mean flow properties, *Journal of Fluid Mechanics,* 711, 2012, 437–468.
[13] Dai, Q., Jin, T., Luo, K., Fan, J., Direct numerical simulation of particle dispersion in a three-dimensional spatially developing compressible mixing layer, *Physics of Fluid*, 30, 2018, 113301.
[14] Takamure, K., Sakai, Y., Ito, Y., Iwano, K.,Hayase, T., International Journal of Heat and Fluid Flow Dissipation scaling in the transition region of turbulent mixing layer, *International Journal of Heat and Fluid Flow*, 75, 2019, 77–85.
[15] Shi, F., Gao, Z., Jiang, C., Lee, C.H., Numerical investigation of shock-turbulent mixing layer interaction and shock-associated noise, *Physics of Fluids*, 33, 2021, 025105.
[16] Chong, D., Bai, Y., Zhao, Q., Chen, W., Yan, J., Hong, Y., Direct numerical simulation of vortex structures during the late stage of the transition process in a compressible mixing layer, *Physics of Fluids*, 33, 2021, 054108.
[17] Chung, K.M., Investigation on transonic convex-corner flows, *Journal of Aircraft*, 39(6), 2002, 1014–1018.
[18] Zhang, H., Wu, J., Chen, J., Liu, W., Characteristics of Large-Scale Structures in Supersonic Planar Mixing Layer with Finite Thickness, *Advances in Mechanical Engineering*, 6, 2014, DOI:10.1155/2014/878679.
[19] Zhang, H., Liu, W., Wu, J., Flow visualization of the large-scale structures in supersonic mixing layer with a recirculation flow region, *Journal of Visualization*, 19, 2016, 15–19.
[20] Hamedi-Estakhrsar, M.H., Mahdavy-Moghaddam, H., Jahromi, M., Investigation of effects of convergence and divergence half-angles on the performance of a nozzle for different operating conditions, *Journal of the Brazilian Society of Mechanical Sciences and Engineering*, 40, 2018, 353.
[21] Tran, T.H., Ambo, T., Lee, T., Chen, L., Nonomura, T., Asai, K., Effect of boattail angles on the flow pattern on an axisymmetric afterbody surface at low speed, *Experimental Thermal and Fluid Science*, 99, 2018, 324–335.
[22] Tran, T.H., The Effect of Boattail Angles on the Near-Wake Structure of Axisymmetric Afterbody Models at Low-Speed Condition, *International Journal of Aerospace Engineering*, 2020, 2020, 7580174.
[23] Tran, T.H., Ambo, T., Lee, T., Ozawa, Y., Chen, L., Nonomura, T., Asai, K., Effect of Reynolds number on flow behavior and pressure drag of axisymmetric conical boattails at low speeds, *Experiments of Fluids*, 60, 2019, 36.
[24] Goebel, S.G., Dutton, J.C., Experimental study of compressible turbulent mixing layers, *AIAA Journal*, 29, 1991, 538–546.
[25] Barre, S., Bonnet, J.P., Detailed experimental study of a highly compressible supersonic turbulent plane mixing layer and comparison with most recent DNS results: "Towards an accurate description of compressibility effects in supers", *International Journal of Heat and Fluid Flow*, 51, 2015, 324–334.
[26] Tan, J., Zhang, D., Li, H., Hou, J., Detailed experimental investigations on flow behaviors and velocity field properties of a supersonic mixing layer, *Acta Astronautica*, 144, 2018, 30-38.
[27] Zhang, D., Tan, J., Lv, L., Wang, Q., Visualization of flow structures and mixing characteristics induced by forced vibration in supersonic mixing layer, *Journal of Visualization*, 19, 2016, 179–182.
[28] Wang, Q.C., Wang, Z.G., Lei, J., Feng, J.H., Characteristics of mixing enhanced by streamwise vortices in supersonic flow, *Applied Physics Letters*, 103, 2013, 144102.
[29] Abikan, A., Yang, Z., Lu, Y., Computational Analysis of Turbulent Flow over a Bluff Body with Drag Reduction Devices, *Journal of Applied and Computational Mechanics*, 6, 2020, 1210-1219.
[30] Esakki, B., Gokul Raj, P., Yang, L.J., Khurana, E., Khute, S., Vikram, P., Computational fluid dynamic analysis of amphibious unmanned aerial vehicle, *Journal of Applied and Computational Mechanics*, 8(2), 2022, 475-484.
[31] Menter, F.R., Lechner, R., Matyushenko, A., Best practice: generalized k-ω two-equation turbulence model in ANSYS CFD (GEKO), *ANSYS Ger. GmbH*, 2019.
[32] Duc, M.B., The, H.T., Van, K.P., Le, A.D., Predicting aerodynamic performance of savonius wind turbine: An application of generalized k-ω turbulence model, *Ocean Engineering*, 286, 2023, 115690.
[33] Larsson, J., Kawai, S., Bodart, J., Bermejo-Moreno, I., Large eddy simulation with modeled wall-stress: recent progress and future directions, *Mechanical Engineering Reviews*, 3, 2015, 15-00418.
[34] Zhang, Y., Wang, B., Zhang, H., Xue, S., Mixing Enhancement of Compressible Planar Mixing Layer Impinged by Oblique Shock Waves, *Journal Propulsion and Power*, 31, 2015, DOI: 10.2514/1.B35423.
[35] Berkooz, G., Holmes, P., Lumley, J.L., The proper orthogonal decomposition in the analysis of turbulent flows, *Annual Review of Fluid Mechanics,* 25, 1993, 539–575.
[36] Moayyedi, M.K., Extension ability of reduced order model of unsteady incompressible flows using a combination of POD and Fourier modes, *Journal of Applied and Computational Mechanics*, 5, 2019, 1–12.
[37] Kim, K.U., Elliott, G.S., Dutton, J.C., Compressibility Effects on Large Structures and Entrainment Length Scales in Mixing Layers, *AIAA Journal*, 58, 2020, 5168–5182.

ORCID iD

Trung Dung Nguyen https://orcid.org/0009-0008-5460-2580
Dinh Anh Le https://orcid.org/ 0000-0001-7121-6894
Van Minh Do https://orcid.org/ 0000-0001-7530-2183
Anh Tuan Nguyen https://orcid.org/ 0000-0002-9235-4759
The Hung Tran https://orcid.org/ 0000-0003-1223-0834

How to cite this article: Nguyen T.D., et al., Effect of Splitter Angles on Characteristics of Mixing Layer Flow: A Numerical Study, *J. Appl. Comput. Mech.*, 11(1), 2025, 39-54. https://doi.org/10.22055/jacm.2024.46204.4480